PNAS
www.pnas.org

Supplementary Information for

Decadal increase in Arctic dimethylsulfide emission

Martí Galí, Emmanuel Devred, Marcel Babin, Maurice Levasseur

Corresponding author: Martí Galí
Email: marti.gali.tapias@gmail.com

This PDF file includes:

Supplementary text
Figs. S1 to S8
Tables S1 to S3
References for SI reference citations

www.pnas.org/cgi/doi/10.1073/pnas.1904378116

Supplementary Information Text

Outline

1. Datasets

1.1 In situ datasets. In situ concentrations of dimethylsulfide (DMS, nM), total dimethylsulfoniopropionate (DMSPt, nM) and chlorophyll *a* (Chl, mg m^{-3}), accompanied by other ancillary data (bottom depth, temperature, salinity), were downloaded from the Pacific Marine Environmental Laboratory database (PMEL; https://saga.pmel.noaa.gov/dms/; last access 13 April 2017). This public dataset contains around 50,000 measurements made between 1972 and 2012, of which around 15,000 were made at latitudes >45°N. We extended it with 9 additional datasets obtained in Arctic and Subarctic waters in recent years (Table S1). We selected measurements from depths shallower than 10 m, deemed representative of the upper mixed layer, 95% of which were taken between 1 and 6 m depth. We then applied quality control criteria to the ensemble data set as described in previous studies (1) and ref. (17) of the main text. Overall, only 0.24% of the measurements were removed through the quality control process. A summary of in situ data availability during the satellite observation period (1998-2016) is given in Table S2.

In situ data were binned to 8-day periods and 27.84 km x 27.84 km pixels to match the resolution of the modeled DMS fields (SI section 2.2). Binning of in situ data gave more even weight to different DMS datasets that had been acquired at different sampling frequencies (Table S2): from discrete measurements from Niskin bottle samples analyzed using purge-and-trap gas chromatography (generally with daily frequency), to automated ship underway systems (with sampling frequencies of up to 1 Hz). Different in situ datasets were binned separately, even if they overlapped in space and time, to keep track of the different methods used. Nevertheless, overlap occurred only in 4.3% of bins, meaning that repeat observations for a given 27.84 km macropixel and 8-day period were scarce. The binned database is made available through a public repository (https://doi.org/10.5281/zenodo.3243967)

Within each bin, the mean, minimum, maximum and data counts were recorded for each variable. For DMS, the median (geometric mean) data counts per documented bin were 3 (3.5); for

DMSPt, 2.0 (1.7); and for Chl, 1.0 (1.5). The best-documented bins, defined as the 95% percentile of bin data counts, contained N > 61, N > 5 and N > 4 measurements for DMS, DMSPt and Chl, respectively.

The binned dataset was used for model tuning and validation (SI section 3). The mean (min–max) concentrations were 5.5 nM (0.05–96.8) for DMS, 41.2 nM (1.0–240.6) for DMSPt, and 1.27 mg m^{-3} (0.03–20.8) for Chl, which illustrates the wide environmental range covered by the dataset. For DMS, the coefficient of variation about the mean was less than 50% in 90% of the bins, suggesting that intra-bin variability was appropriate. Most measurements (67%) were taken between May and August, our period of interest.

The sea-surface DMS climatology produced by Lana et al. (2011) was downloaded from http://www.bodc.ac.uk/solas_integration/implementation_products/group1/dms/. This 1°x1° monthly climatology is based on the sea-surface DMS measurements available on the PMEL website (https://saga.pmel.noaa.gov/dms/; last update April 2010; accessed 13 April 2017), covering the period 1972-2009, and will be referred hereafter as L11. We interpolated the L11 climatology to 8-day periods and re-projected it onto a 27.84 km grid to allow for direct comparison against the output of our algorithm.

1.2 Ocean color and ancillary geophysical data. Ocean color datasets were downloaded from the NASA ocean color website (https://oceancolor.gsfc.nasa.gov/) for two satellite sensors: the Sea-viewing Wide Field-of-view Sensor (SeaWiFS; 9.28 km resolution) and the Moderate Resolution Imaging Spectroradiometer onboard the Aqua satellite (MODIS-Aqua; 4.64 km resolution) (2). SeaWiFS data covered the period 1998-2007 (the SeaWiFS record is discontinuous after 2007), and MODIS-Aqua the period 2003-2016, with 5 years of overlap (2003-2007). We used the 2014.0 reprocessing for both missions to maximize consistency. The following variables (level-3 binned data) were downloaded and used to compute other variables or for data analysis: daily composites of remote sensing reflectance spectra (Rrs(λ)) and 8-day composites of mean daily photosynthetically available radiation (PAR; mol photons m^{-2} d^{-1}). Daily ocean color data is the basis of our processing chain (SI section 2.1) and defines the primary amount of observations available to calculate DMS concentration fields.

Mixed layer depth (MLD) was obtained from the monthly isopycnal/mixed-layer ocean climatology (MIMOC; http://www.pmel.noaa.gov/mimoc/) with 0.5°x0.5° resolution (3).

Daily sea ice concentration (SIC) at 25 km x 25 km resolution was downloaded from the National Snow and Ice Data Center. Sea ice concentration data from ref. (4) was used for 2002 to 2015, corresponding to the sensors SMMR on the Nimbus-7 satellite and SSM/I-SSMIS on DMSP satellite platforms (http://nsidc.org/data/NSIDC-0051/versions/1). Sea ice concentration data from ref. (5) was used for 2016, corresponding to the sensor SSMIS on DMSP satellite platforms (http://nsidc.org/data/NSIDC-0081/versions/1).

Sea surface temperature (SST) and the eastward (u) and northward (v) components of 10-m height wind speed (WS) were obtained from the ERA-Interim reanalysis (6) for the period 1998-2016 (data downloaded from the ECMWF data server). We used the daily analysis data at 12 UTC. The WS modulus was calculated by adding in quadrature the u and v components.

Daily satellite-observed gridded SST (12-µm wavelength) was also obtained from the Advanced Very High Resolution Radiometer (AVHRR) for the period 1998-2012, Pathfinder Version 5.3 (https://climatedataguide.ucar.edu/climate-data/sst-data-avhrr-pathfinder-v53-noaa-nodc). For the period 2003-2016 we supplemented AVHRR data with MODIS-Aqua nighttime SST (11-µm

wavelength; https://oceancolor.gsfc.nasa.gov/) to maximize coverage. These products were used in the DMSPt processing chain because their resolution matches that of ocean color data.

A monthly climatology of sea surface salinity was obtained from the World Ocean Atlas 2013 (WOA13 v2; https://www.nodc.noaa.gov/cgi-bin/OC5/woa13/woa13.pl?parameter=s) for the period 2005-2013.

Bathymetry was obtained from the General Bathymetric Chart of the Oceans (GEBCO_2014, http://www.gebco.net/data_and_products/gridded_bathymetry_data/). North of 64°N, GEBCO_2014 incorporates the International Bathymetric Chart of the Arctic Ocean (IBCAO 3.0) released in 2012.

When needed, the datasets were re-projected onto the sinusoidal equal-area grids used in our remote sensing processing chain (4.64 km × 4.64 km pixels for MODIS-Aqua; 9.28 km × 9.28 km pixels for SeaWiFS; and 27.84 km × 27.84 km macropixels for DMS and FDMS variables) and/or binned to 8-day periods. Monthly MLD was also linearly interpolated to 1-day resolution. Maps of the processed and the original datasets were visually compared and no significant alterations were detected. In the case of the MLD, salinity and L11 DMS climatologies, the coarse spatial resolution of the original datasets produced data gaps in coastal areas. These gaps were filled using the nearest available measurements to obtain full coverage prior to computing sea-air DMS fluxes.

2. Remote sensing processing chain

The DMS_{SAT} algorithm proceeds through two steps, the DMSPt and DMS sub-algorithms, which embody macroecological patterns that regulate sea-surface DMS concentration. Below we describe the implementation of the algorithm for northern high latitudes.

2.1 Ocean color data and DMSPt sub-algorithm. We computed chlorophyll *a* (Chl; mg m^{-3}) concentration from daily Rrs(λ) using different types of algorithms: the semi-analytical Garver-Siegel-Maritorena (GSM) (7) algorithm, and standard band-ratio algorithms (8) for SeaWiFS and MODIS (generically called OC). These Chl products will hereafter be referred to as Chl_{GSM} and Chl_{OC}, respectively. The GSM algorithm can retrieve simultaneously the absorption coefficients of phytoplankton pigments (a_{phy}) and colored detrital matter (a_{CDM}), and the particle backscattering coefficient. The Chl concentration, which is derived from a_{phy}, is less affected by interference from high CDM abundance in optically complex waters. Thus, GSM is a priori more appropriate in waters with continental runoff influence, and has been show to outperform OC in Beaufort Sea coastal waters (9). On the other hand, the GSM algorithm relies on absolute reflectance spectra and is therefore more sensitive to errors in atmospheric correction compared to band-ratio OC algorithms. Here *we chose GSM as our default algorithm*, and compared its results to OC-derived data to ensure robustness in open ocean waters.

We computed diffuse attenuation coefficients of downwelling irradiance ($K_d(\lambda)$; m^{-1}) at wavelengths (λ) of 490 nm for SeaWiFS and 488 nm for MODIS Aqua from daily Rrs(λ) spectra using the algorithm of Lee et al. (10). We then calculated euphotic layer depth (Z_{eu}; m) as the depth of 1% penetration of 490 or 488 radiation, as $Zeu = 4.6/K_d(\lambda)$.

We computed daily maps of sea-surface DMSPt using the algorithm of Galí et al. (1). A total of four DMSPt datasets were generated, corresponding to the two sensors (SeaWiFS or MODIS Aqua) and the two Chl products (Chl_{GSM} or Chl_{OC}) for each sensor. The DMSPt algorithm switches between two equations two different equations depending on the quotient between euphotic layer depth (Z_{eu}; 1% light penetration) and mixed layer depth (MLD):

$\log_{10}DMSPt = 1.70 + 1.14\ \log_{10}Chl + 0.44\ (\log_{10}Chl)^2 + 0.063\ SST - 0.0024\ SST^2$,
$Z_{eu}/MLD \geq 1$ (eq. 1a)

$\log_{10}DMSPt = 1.74 + 0.81\ \log_{10}Chl + 0.60\ \log_{10}(Z_{eu}/MLD)$,
$Z_{eu}/MLD < 1$ (eq. 1b)

(Chl in mg m^{-3}, SST in °C, Z_{eu} and MLD in m). These equations implicitly represent DMSPt concentration in phytoplankton communities dominated by different taxonomic and size classes. Eq. 1a reflects pico- and nanoplankton dominated waters with a prominent role for prymnesiophytes (e.g. *Phaeocystis* sp.) and high DMSPt:Chl ratios (typically of order 100 µmol μg^{-1}). Eq. 1b reflects microplankton dominated waters with a prominent role for diatoms and low DMSPt:Chl ratios (typically <30 µmol μg^{-1}). Here *we used the model coefficients optimized for the global ocean*, which performed well in Arctic and Subarctic waters (see SI section 3). From May through August (our period of interest), $Z_{eu}/MLD > 1$ occurs in about 90% of observed pixels in the Subarctic and Arctic seas (*stratified* condition, eq. 1a).

In pixels where satellite Chl cannot be retrieved because of coccolith-enhanced light scattering, i.e. in decaying cocclithophore blooms, the DMSPt algorithm proposed a third equation based on satellite-retrieved PIC. This equation was not used in our study to avoid PIC retrieval artifacts in coastal waters (11).

2.2 Binning and gap-filling scheme and DMS sub-algorithm. On average, less than 10% of ice-free marine pixels are documented daily by ocean color satellites in our study domain because of cloud cover (Fig. S1). Yet, full coverage is required prior to DMS and FDMS calculation to (i) avoid positive PAR bias towards cloud-free pixels (see eq. 2 below), and (ii) allow for full interaction between DMS, wind speed and SST fields when computing FDMS (see SI section 4). Therefore, we applied a stepwise binning and gap-filling scheme to obtain full DMSPt and DMS coverage, excluding areas that cannot be observed due to low solar elevation during the polar winter, finally resulting in a temporal resolution of 8 days and a spatial resolution of 27.84 km ("28 km" equal-area sinusoidal grid). The increase in coverage through the binning and gap-filling process, and its seasonal variation, is shown in Fig. S1 and briefly described below.

First, daily data were binned to 8-day periods and 27.84 km macropixels (which comprise 3x3 SeaWiFS and 6x6 MODIS-Aqua level 3 pixels), increasing areal coverage from 10-11% to 62-71%; second, remaining empty pixels were filled by linear temporal interpolation, achieving ~90% coverage; finally, the 10% remaining pixels were successively filled with the 8D and the monthly climatology of each sensor to achieve full coverage. These proportions refer to ice-free marine pixels only, and the ranges reflect variations depending on the sensor.

The spatial-temporal resolution of the binned data was chosen after preliminary tests consisting of spatial-temporal variograms. In the spatial domain, the 28 km spatial resolution preserves large-scale gradients while smoothing out mesoscale variability —eddies at (sub)polar latitudes are smaller than this macropixel size. In the temporal domain, the 8-day resolution retains the sharp phytoplankton biomass peaks characteristic of high latitudes that would be smoothed out using monthly temporal averaging. Finally, sea-surface DMS was estimated as a function of satellite-retrieved DMSPt and PAR, binned to 28 km and 8-day periods, according to eq. 2 of the main text.

Sea-surface DMS concentration (nmol L^{-1}) was estimated from 8-day 28 km DMSPt and PAR as:

$\log_{10}(DMS) = -1.30 + 0.70 \log_{10}(DMSPt) + 0.020\ PAR$ (eq. 2)

3. DMS_{SAT} algorithm tuning and skill metrics

As explained above, we estimated DMSPt using the coefficients optimized for the global ocean (eq. 1a and 1b). This is justified because DMSPt sub-algorithm skill metrics in our full study domain (>45°N) were similar to those reported for the global ocean (1), with RMSE ~ 0.30 and R^2 ~ 0.50 for $\log_{10}$DMSPt. Additional preliminary tests of the DMSPt sub-algorithm north of 45°N included the use of alternative satellite Chl algorithms (9, 12), different narrow-band or integral-band K_d for the estimation of Z_{eu}, and different MLD products. Overall, these tests indicated (i) little sensitivity to Z_{eu} and MLD choices, and (ii) best performance with Chl_{GSM} and Chl_{OC} compared to regional Arctic algorithms (9, 12). We also tested the DMSPt sub-algorithm using recent measurements acquired during the Green Edge 2016 cruise in Baffin Bay (Galí et al. dataset in Table S2) that were not used in algorithm development. The Green Edge cruise sampled the ice margin phytoplankton bloom, with phytoplankton biomass dominated by either *Phaeocystis pouchetii* or diatoms and DMSPt ranging between 10 and 300 nM. This test also produced favorable validation statistics (RMSE ~ 0.29 and R^2 ~ 0.44 for $\log_{10}$DMSPt).

After thorough testing, and given higher availability of in situ DMS data (Table S2) with concurrent satellite matchups, we focused on adjusting the DMS sub-algorithm coefficients (eq. 2) for Subarctic and Arctic Ocean waters. The reader is referred to references (1) and ref. (17) of the main text for a detailed discussion of algorithm skill metrics and their dependence on (i) the satellite sensors used (SeaWiFS or MODIS-Aqua), (ii) the Chl products used (GSM and OC), (iii) the degree of data binning, and (iv) the availability of in situ Chl data to constrain the error in satellite-retrieved Chl.

The DMS sub-algorithm (eq. 2) coefficients used here are based on a regression analysis of 5°x5° monthly binned data (DMS, DMSPt and PAR) for latitudes >45°N (ref. 17 of the main text). This regression involved only data bins where both in situ DMS and DMSPt were available (20% of bins). To further constrain the ranges of variation of eq. 2 coefficients, we used the bootstrap method to produce 10^5 sets of regression coefficients (Fig. S2). Based on this analysis, *eq. 2 coefficients were further adjusted for latitudes >45°N using the 28 km 8-day binned DMS dataset* (SI section 1). After comprehensive tests, we set these coefficients to optimal values of $\alpha = -1.30$, $\beta = 0.70$ and $\gamma = 0.020$. Our tests took into account both (i) the trade-offs between the minimization of RMSE and the maximization of the models' ability to reproduce the full spread of the data (13) and (ii) the visual inspection of validation scatterplots (Fig. S3) and DMS seasonal cycles (Fig. 1 of the main text). For the latter analysis we considered both the full domain and specific Arctic and Subarctic ecoregions. These ecoregions were chosen based on their distinct DMS dynamics and the availability of in situ DMS data, and their size was adjusted to ensure they represented relatively homogeneous ecosystem dynamics.

Fig. S3 shows validation statistics for our reference algorithm configuration for the MODIS-Aqua satellite record (2003-2016). It is important to note that these statistics are based on a dataset much larger than that used for algorithm development, because:
(i) Only pixels containing both DMS and DMSPt data were used for algorithm development (20% of 5°x5° monthly pixels, 12% of 8-day 28 km pixels), and
(ii) Validation statistics include pixels where the binning and gap-filling procedure was applied, increasing by about 50% the amount of pixels available in a "strict" satellite matchup assessment.
The DMS_{SAT} algorithm calibrated for Subarctic and Arctic latitudes estimates in situ $\log_{10}$DMS (8-day 28 km binned data; Table S2) with RMSE = 0.40, bias = 4%, $R^2 = 0.41$, and model:data slope = 0.85 (type II major axis regression). With this validation dataset, DMS_{SAT} has skill similar to the objective interpolation-based climatology of Lana et al. (L11) (ref. 16 of the main text). In

particular, DMS_{SAT} has very similar RMSE, lower bias, and a model:data slope closer to 1, with the obvious advantage that DMS_{SAT} allows for interannual variation.

We also compared DMS_{SAT} and L11 using the ST score proposed by Jollif et al. (13). This skill score takes into account the mean-normalized variance, the correlation coefficient and the bias of model estimates against observations. Quoting Jollif et al., "the contrast between the ST score and the total RMSD [=RMSE] is that the skill score does not reward underestimates of the variance for correlation values less than one". Since lower ST score indicates better model skill, DMS_{SAT} (ST = 0.23) has better performance than L11 (ST = 0.40) according to this metric. Therefore, DMS_{SAT} is better suited to capture DMS variability in space and time. Fig. S3 also shows that the probability distribution of DMS_{SAT} better matches that of in situ data (panel D), such that model-data residuals are more symmetric around 0 (panel E) or, in log_{10} space, the model/data ratio is more normally distributed around 1 (panel F). As thoroughly discussed by Galí et al. (ref. 17 of the main text), the sparseness of in situ data and the sampling bias towards bloom conditions can compromise the objective interpolation procedures used to calculate the L11 climatology. This is particularly true in the Arctic seasonal ice zone, where phytoplankton dynamics follow variable ice retreat patterns.

Fig. S3 shows DMS_{SAT} skill metrics for the MODIS-Aqua record (2003-2016), when strongest changes in Arctic DMS emission were detected. Corresponding DMS_{SAT} skill metrics for MODIS-Aqua *using as input the alternative Chl_{OC} product* were: ST = 0.27, RMSE = 0.41, bias = 11%, R^2 = 0.41, slope = 0.82 (N = 2259). Corresponding DMS_{SAT} skill metrics for SeaWiFS (1998-2007) using as input the default Chl_{GSM} product were: ST = 0.24, RMSE = 0.45, bias = 3%, R^2 = 0.42, slope = 0.83 (N = 1856). This highlights the consistency across sensors.

The performance of DMS_{SAT} can be compared to that of primary production algorithms based on satellite data in the Arctic Ocean. A round-robin study that included 32 net primary production (NPP) models for the Arctic Ocean (14) found an average RMSE of 0.28 for log_{10}(NPP) (0.65 for ln(NPP)), slightly lower than the RMSE = 0.40 obtained for log10(DMS_{SAT}). The mean correlation coefficient to in situ data for modeled log_{10}(NPP) was r = 0.38, substantially lower than the r = 0.64 found for $log_{10}(DMS_{SAT})$ (Figure S3). Therefore, DMS_{SAT} estimates captures more variance than satellite NPP models, but also has somewhat larger uncertainty. Given that DMS_{SAT} relies on macroecological relationships, whereas NPP models use input variables (chlorophyll, PAR) that directly control NPP rates, this comparison supports the remarkable skill of DMS_{SAT}.

Fig. S4 shows pan-Arctic maps of $DMSPt_{SAT}$ and DMS_{SAT} as diagnosed with our algorithm, as well as the ratio between DMS_{SAT} and DMS_{L11} and sea-air gas exchange coefficient K_w.

4. Sea-air DMS flux (FDMS)

FDMS was calculated as the product of a transfer coefficient K_W (m d^{-1}; chiefly controlled by wind speed and sea surface temperature) and the DMS gradient at the interface,

$$FDMS = K_W (DMS_w - DMS_a/H) \qquad \text{(eq. 3)}$$

where DMS_w and DMS_a are DMS concentrations (µmol m^{-3}) in surface seawater and the air overlying it, respectively, and H is the dimensionless gas-over-water Henry's law solubility. Since seawater is generally largely supersatured with DMS, i.e. $DMS_w >> DMS_a/H$, many studies omit the DMS_a/H term. Here we estimated DMS_a as a constant fraction of DMS_w, $DMS_a = DMS_w$ / 252.75. This constant is based on four North Atlantic cruises at latitudes between 43°N and 54°N, which displayed a C_w/C_a ratio (mean ± std) of 252.75 ± 61.02 (see Table 1 in ref. (15)). Failing to

account for the DMS_a/H term would overestimate DMS emission by 8% at SST = 5°C and salinity = 34. We calculated H using the numerical scheme of Johnson (16), which includes both temperature and salinity effects on gas solubility.

The total DMS transfer coefficient K_w was calculated considering boundary layers on both sides of the sea surface:

$$K_w = (1/k_w + 1/(k_a \times H))^{-1} \qquad \text{(eq. 4)}$$

where k_w and k_a are the water-side and air-side transfer coefficients, respectively (17). Although waterside resistance ($r_w = 1/k_w$) largely controls the exchange of sparingly soluble gases like DMS, air-side resistance ($r_a = 1/k_a$) may decrease total K_w by 5–10% depending on wind speed and temperature conditions, and has to be taken into account. We calculated k_a using the numerical scheme of Johnson (16), which builds on the NOAA COARE algorithm and improves it in the low wind speed range (16, 18). Johnson's code was also used to calculate normalized $k_{w,600}$ (the k_w of CO_2 at 20°C in freshwater), which was then scaled to DMS diffusivity using the dimensionless Schmidt number raised to -1/2 ($Sc^{-1/2}$) (19). We modified Johnson's code to calculate Sc according to the DMS diffusivity parameterization of Saltzman et al. (20).

We used two different models to parameterize the water-side transfer coefficient k_w. Although both models use wind speed at 10 m height (WS) as the physical driver of gas exchange, they differ in their physical foundations. The first is the widely used empirical parameterization of Nightingale et al. (2000) (21), (hereafter N00), based on dual tracer gas exchange measurements. The second is the physically-based scheme of Woolf (1997) (22) (hereafter W97), which includes two terms: (i) turbulence-mediated gas exchange, represented as a function of wind stress (in turn a function of WS and the drag coefficient); and (ii) bubble-mediated gas exchange, represented as a function of the whitecap fraction (in turn parameterized as a function of $WS^{3.41}$).

The difference between the two schemes is small at WS <10 m s^{-1}, whereas at WS >10 m s^{-1} the N00 scheme produces higher k_w owing to its quadratic form (Fig. S5A). At intermediate wind speeds (5–10 m s^{-1}), which account for about 60% of DMS emission in our domain (Fig. S5C), the W97 scheme has nearly linear behavior, in better agreement with direct DMS flux measurements based on the eddy correlation technique (Fig. S5A). Bubble-mediated gas transfer is small for moderately soluble gases like DMS, which is also in support of gas transfer schemes with nearly linear behavior. For instance, at high WS of 20 m s^{-1}, the W97 scheme predicts a 20% enhancement of DMS K_w due to bubbles, but this K_w is still ~25% lower than that estimated with N00. For these reasons here *we adopted W97 as our default parameterization*.

In our processing chain, the K_w and H for a given pixel were linearly interpolated from pre-computed look-up tables (LUT). The K_w LUT had 136,500 elements, resulting from 100 wind speed levels (0.25-25 m s^{-1}), 65 SST levels (-2 to 30 degrees) and 21 salinity levels (0 to 40), all divided at regular intervals. The H LUT had 1,365 elements, resulting from 65 SST levels (-2 to 30 degrees) and 21 salinity levels (0 to 40). Fig. S5B illustrates the important effect of SST on K_W and the small effect of salinity.

Daily FDMS was computed from daily wind speed and SST from the ERA-Interim reanalysis and 8-day DMS fields (eq. 3). FDMS was then averaged over 8-day periods for data analysis. We used instantaneous wind speed values taken daily at 12:00 hours (ERA-Interim), avoiding temporal averaging prior to FDMS calculation, to preserve wind speed variability (23). Fig. S6 shows seasonal cycles of FDMS in selected Arctic ecoregions matching those in Fig. 1 of the main text.

5. Assessment of uncertainty in DMS emission

We produced alternative DMS emission time series to evaluate different sources of uncertainty. The mean satellite-based EDMS in summer between years 2003 and 2016 (MODIS-Aqua record) was 114±10 and 53±11 Gg S for the 60-70°N and >70°N latitude bands, respectively, for our reference configuration ("reference run"). Using an alternative chlorophyll product (Chl_{OC}; SI setion 2.1) gave similar emissions of 127±7 and 51±9 Gg S for the same latitude bands. Replacing satellite-based DMS with the Lana et al. DMS climatology gave slightly higher estimates of 140±5 and 72±9 Gg S. When we used an alternative gas exchange parameterization in combination with our reference DMS_{SAT} fields, we obtained similar EDMS of 115±10 and 53±11 Gg S for the 60-70°N and >70°N latitude bands. The overall good agreement between different datasets suggests our EDMS estimates are robust. Finally, mean EDMS in the 60-70°N band computed with our reference configuration was extremely similar during the SeaWiFS observation period (1998-2007; 111±10 Gg S) and the MODIS-Aqua observation period described above (2003-2016; 114±10 Gg S). This suggests stable EDMS in the 60-70°N region, which was minimally affected by changes in sea ice extent over the study period.

Uncertainty in EDMS trends was analyzed in latitudes north of 70°N and for the MODIS-Aqua 2003-2016 record, which largely determine the outcomes of our study. These alternative algorithm runs are described below and their main results are compiled in Table S3, where we report multiyear means and trends, and the mean percentage deviation (MPD) and mean absolute percentage deviation (MAPD) of annual summer values with respect to the reference run (named ***0. REF***).

1. COEFFS: in this run we assessed the sensitivity to eq. 2 coefficients (DMS sub-algorithm). We produced an ensemble of 10 FDMS datasets, each derived from a different set of eq. 2 coefficients. The 10 sets of eq. 2 coefficients were randomly selected from a larger set of 10^5 bootstrapped coefficients (as shown in Fig. S2), and adjusted for the mean difference between the regression-derived coefficients (α = -1.28, β = 0.67 and γ = 0.0186) reported by Galí et al (ref. 17 of the main text) and the optimized coefficients employed here in the reference run (α = -1.30, β = 0.70 and γ = 0.0200). We then calculated a composite EDMS time series resulting from averaging the ensemble of 10 EDMS time series. The composite time series showed virtually the same multiyear means and trends as the reference run. The mean coefficient of variation about the EDMS ensemble annual means was ± 8.5%.

2. CHLOC: we replaced Chl_{GSM} by Chl_{OC} to assess the sensitivity of EDMS to input satellite Chl products. Although mean 2011-2016 EDMS was very similar to the reference run, the 2003-2016 trend was 22% faster (though non significantly). The largest negative (positive) deviations compared to ***REF*** were recorded in 2011 (2016), with -18% (+24%).

3. KW: we replaced K_w derived from the W97 parameterization with K_w derived from the N00 parameterization. This change decreased annual EDMS by 1.7% on average. However, the 2003-2016 trend was 8% faster with N00 (though non significantly). This suggests that the trend derived from W97 K_w is, if anything, conservative, and less sensitive to the slight increase in wind speed recorded in recent years (see Fig. 4 of the main text).

4. REF.CLIM: we replaced time-varying DMS fields by the DMS_{SAT} climatology (8-day 28 km resolution), calculated from the reference run. This had a small impact on mean annual EDMS but increased the 2003-2016 trend by 39% (though non significantly). The largest negative (positive) deviations compared to ***REF*** were recorded in 2011 (2016), with -13% (+39%). Thus,

EDMS deviations associated to the use of satellite-derived climatological fields were similar or larger than those associated to the different satellite Chl products tested.

5. L11.CLIM: we replaced time-varying DMS fields by the L11 climatology (interpolated to 8-day resolution and re-projected onto the 28 km grid). This change gave on average 37% higher EDMS. The 2003-2016 increasing trend was 18% faster than ***REF*** (though non significantly). Since L11 displays lower DMS in coastal areas and higher DMS in the Central Arctic basin compared to ***REF*** (Fig. S4), this analysis shows that the DMS deviation in the Central Arctic dominates differences in pan-Arctic EDMS estimates and its trends.

Comparison of the reference run (***REF***) with either ***REF.CLIM*** or ***L11.CLIM*** suggests EDMS trends are somewhat sensitive to the use of climatological fields, but uncertainty is generally within the 95% CI of our ***REF*** trends. A priori, combination of time-varying DMS fields with concurrent meteorological observations (***REF***) should yield the most realistic estimates.

6. Decomposition of interannual EDMS variations

We adapted the analysis of Vancoppenolle et al. (ref. 5 of the main text) to decompose EDMS changes into the following components:

1. Change in mean FDMS over a common domain, that is, in grid elements (pixels-periods) that were ice-free in any given consecutive years (y1 and y2).
2. Change associated to different spatial-temporal ice cover patterns, divided into:
    a. Gained EDMS: pixels documented in y2 and not in y1 in a given 8D period.
    b. Lost EDMS: pixels documented in y1 and not in y2 in a given 8D period.

To calculate these components, the FDMS matrices of each year (m x n, where m is pixel index and n is time) were converted to column vectors (of size m*n x 1). Then, for each couple of consecutive years we defined three subsets:

O: common ocean pixels, with SIC < 10% in both y1 and y2.
G: pixels gained, with SIC ≥ 10% in y1 and SIC < 10% in y2.
L: pixels lost, with SIC < 10% in y1 and SIC ≥ 10% in y2.

EDMS from common ocean pixels, $EDMS^O$, was calculated as the product of mean $FDMS^O$ and the corresponding area, A^O in each year,

$$EDMS^O_y = < FDMS^O_y > A^O \qquad \text{(eq. 5)}$$

Note that A^O was equal in both years since the pixel-time elements were common. Component 1 of EDMS was then calculated as:

$$\Delta EDMS^O = EDMS^O_2 - EDMS^O_1 \qquad \text{(eq. 6)}$$

Component 2a was calculated as the summation of FDMS over the G domain in year 2 (since in year 1 the domain G produced no emissions):

$$\Delta EDMS^G = \Sigma FDMS^G_2$$

Similarly, component 2b was calculated as the summation of FDMS over the L domain in year 1 (since in year 2 the domain L produced no emissions):

$$\Delta EDMS^L = -\Sigma FDMS^L_1$$

The net EDMS change caused by shifts in ice patterns is:

$\Delta EDMS^{ICE} = \Delta EDMS^{G} - \Delta EDMS^{L}$

And the net interannual change is:

$\Delta EDMS = \Delta EDMS^{O} + \Delta EDMS^{ICE}$

This analysis is graphically summarized in Fig. S7. As an additional check, it can be seen that ΔEDMS calculated in this way matches the net interannual EDMS changes shown in Fig. 4 of the main text. A regional breakdown of EDMS time series and their drivers is shown in Fig. S8.

7. Review of DMS emission projections and their radiative effects

Here we provide a brief and non-exhaustive review of previous projections of Arctic EDMS under climate change scenarios and the corresponding effects on aerosols and the radiation budget, following a chronological order. Note however that different projections can be hardly compared because they focused on different domains, and the Earth System models (ESMs) used in different studies differed in the degree of coupling between ocean physics, sea ice dynamics, ocean biogeochemistry, atmospheric chemistry, aerosols and cloud microphysics. Finally, note that there is an important vertical asymmetry in the shortwave and longwave components of cloud radiative forcing (CRF_{SW} and CRF_{LW}, respectively). CRF_{SW} at the top-of-atmosphere (TOA), the value reported by most modeling studies, is in general only slightly less than at the sea surface. However, CRF_{LW} at the TOA is much smaller than at the surface. In consequence, indirect aerosol effects on clouds at very low CCN concentrations can warm the surface while cooling the TOA (see figure 2 in ref. 33 of the main text and corresponding text explanations).

Gabric et al. (2005) (ref. 21 of the main text) used an ESM with interactive ocean physics, sea ice, biology and sulfur biogeochemistry. They reported that significant decreases in sea-ice cover (61% in summer–autumn), increases in mean annual SST of 1°C, and a shoaling of the mixed layer depth by 13%, would result in annual DMS flux increases of over 80% in the 70°N-80°N latitude band by 2080 (in response to a tripling of atmospheric CO_2). Their estimated rate of EDMS increase, about 11% $decade^{-1}$, is one third of our contemporaneous satellite-based estimates. This is coherent with slower-than-observed ice loss rates in their model. Using a crude representation of DMS effects on CCN and cloud albedo (probably unrealistic in the Arctic) they estimated a DMS-driven CRF_{SW} of –7.6 W m^{-2}.

Browse et al. (2014) (ref. 26 of the main text) used the Global Model of Aerosol Processes (GLOMAP-mode) with uncoupled meteorology and atmospheric oxidants, and represented sea-surface DMS using the climatology of Kettle et al. (1999) (24). This climatology suffers from data sparseness in the Arctic even more than its successor L11. Browse et al. projected a 15-fold increase in EDMS north of 70°N in August in response to complete sea ice loss, which is unrealistic according to our study. They found an increase in nucleation rates but a weak CCN response due to efficient aerosol scavenging by drizzling stratocumulus clouds. They also suggested an alternative scenario whereby increasing CCN would suppress precipitation (thus increasing cloudiness and albedo). They did not estimate the associated radiative effects, but highlighted the spatial heterogeneity of aerosol responses in their model.

Ridley et al. (2016) (ref. 3 of the main text) used an ESM with coupled ocean, sea ice and atmosphere (HadGEM2-ES). However, marine sulfur biogeochemistry was not included in their

model, and sea-surface DMS was diagnosed within the ESM using the empirical algorithm of Simó and Dachs (2002) (25) (hereafter SD02), based on chlorophyll and mixed layer depth. They projected a 2- to 5-fold increase in "high-Arctic" EDMS in response to total sea ice loss (in their study the "high Arctic" domain has a variable latitudinal limit, located at about 70°N in the Bering Strait and 80°N in the Svalbard sector). Their estimates lie in the upper end of ours, probably because the SD02 algorithm overestimates Arctic DMS in summer and early fall (ref. 17 of the main text). DMS overestimation in SD02 results from it being parameterized as a function of oceanic mixed layer depth, combined with shallow salinity stratification in the Arctic. Thus, the SD02 scheme also overemphasizes the DMS response to projected mixed layer shoaling in the Arctic. The DMS-driven CRF_{SW} was estimated at between –1 and –2 W m^{-2}, but DMS-driven CRF_{LW} was not estimated.

Mahmood et al. (2019) (ref. 24 of the main text) used the CanESM4.3 model, with coupled ocean, sea ice and atmosphere, but represented DMS non-interactively using different climatological fields: the L11 climatology, a preliminary version of our satellite-based climatology (which had lower mean DMS concentration that the version presented here), and spatially uniform DMS concentration. Thus, in their model EDMS changed only in response to ice cover, SST and wind fields. They found that a 25% reduction of summer ice cover (latitudes >62.78°N) increased DMS emission by 33–46% (7–9% $decade^{-1}$) between 2000 and 2050. Their rate of EDMS increase is about 50% slower than our satellite-based estimates for the same latitude band, owing to slower-than-observed ice receding in the model. Although the sulfate burden does not increase proportionally due to increased scavenging, they project a major increase in nucleation rates (3– to 4–fold) that heightens cloud droplet number concentrations. The pan-Arctic DMS-driven annual mean CRF_{SW} is –0.14 W m^{-2}, but this average hides large spatial heterogeneity, with local CRF_{SW} generally ranging ±1.6 W m^{-2}, as well as seasonal variability (which is not addressed). No results are given regarding CRF_{LW}.

Besides the Arctic-focused studies reviewed above, below we briefly review other studies that had a global scope. They do not provide detailed information on the relationship between Arctic EDMS, ice cover, aerosols and radiative forcing, but add interesting nuances regarding DMS-climate feedbacks, like the potential impact of ocean acidification or phytoplankton species shifts.

Six et al. (2013) (ref. 38 of the main text) used the MPI-ESM, with interactive ocean physics, sea ice, marine biology and sulfur cycle, and an offline model for cloud microphysics (ECHAM5.5-HAM2). Additionally, they represented within MPI-ESM the potential response of DMS to ocean acidification. To do so, they extrapolated scenarios derived from weeks-long experimental studies to the global scale and over the next century. Their estimated DMS-driven radiative forcing at the TOA (due to both aerosols and clouds) under a climate change scenario (2090-2099 vs. pre-industrial period) ranges from about 0 W m^{-2} at 70°N to between –1 and –2 W m^{-2} north of 75°N. Although Arctic EDMS increases in response to sea ice loss in all of their ocean acidification scenarios, the EDMS increase (and its radiative effect) becomes smaller with increasing acidification. A follow-up study by Schwinger et al. (2017) (26) obtained similar results using coupled ocean and atmosphere models, which allowed for feedbacks between marine DMS production and climate while better resolving regional responses.

The effect of phytoplankton community species composition was tackled by Wang et al. (2015) (ref. 20 of the main text). They showed that explicit parameterization of *Phaeocystis* sp. (a key DMS producer in polar environments) can improve DMS estimates in a biogeochemical model. The improved model was subsequently used (27) to show that species shifts can influence EDMS and regional and global climate in various ways. In another study (28), they proposed that relevant feedbacks between phytoplankton primary production, DMS emission and climate can

occur at regional and global scales (see also (29)). Therefore, the latter study concluded that "it is necessary to model marine ecosystems dynamically and the marine sulfur cycle explicitly in order to better evaluate the role of DMS in the climate system". Finally, Grandey and Wang (2015) (ref. 39 of the main text), and Fiddes et al. (2018) (29) examined the effects of large EDMS perturbations on modeled present and future climate. They found significant global effects on radiative forcing and precipitation. Fiddes et al. also highlighted the limited capacity of most models to represent the horizontal and vertical distribution of clouds, which implies shortcomings in simulating aerosol-cloud interactions.

From this short review it can be concluded that: (i) the relationships between Arctic Ocean EDMS and ice cover, and their spatial patterns, were poorly constrained in previous model studies; (ii) interannual variability in EDMS and atmospheric processes was not properly (or not at all) represented; (iii) models consistently predict an increase in nucleation rates in response to increased EDMS in the Arctic, (iv) models generally predict an increase in cloud albedo in response to increasing EDMS in the Arctic, but its magnitude and spatial-temporal distribution are uncertain; (v) the response of longwave cloud forcing at the sea surface to increasing EDMS is uncertain. Extreme sensitivity at very low CCN over the Arctic ice pack (ref. 32 of the main text) is generally not considered in detail, perhaps because of the models' limited ability to represent cloud macrophysics (occurrence and lifetime); (vi) atmospheric responses are spatially heterogeneous in the Arctic, and seasonal patterns should also be considered in detail (30); and (vii) potential EDMS changes due to phytoplankton species shifts and acidification are uncertain.

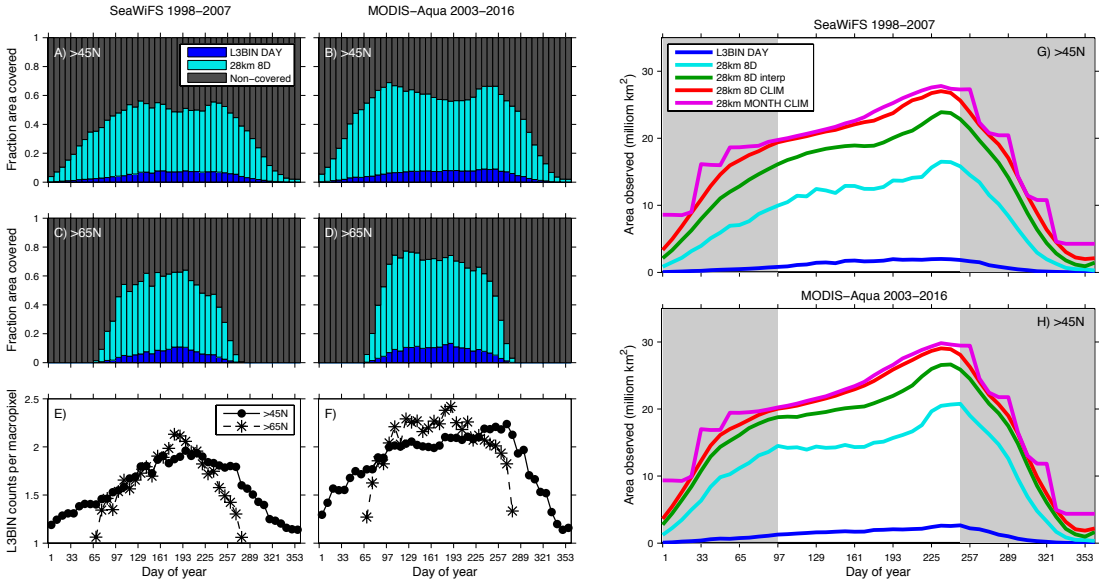

Fig. S1. **Statistics of satellite observations over the seasonal cycle.** A-D) Fraction of the ice-free ocean surface covered by level-3 daily satellite data, and after binning to 8 days and 28 km macropixels, for different sensors (SeaWiFS and MODIS-Aqua) and latitudinal domains (>45°N and >65°N). E-F) number of level-3 daily observations averaged into 8-day 28 km macropixels. G-H) as in (A–D), but in terms of absolute area observed, and showing the sequential binning and gap-filling procedure: 8-day and 28 km binning, temporal interpolation, filling with 8-day satellite climatology, and filling with monthly satellite climatology. These statistics correspond to Chl_{GSM} and its derived DMSPt. In (G–H), gray shading indicates the period when solar elevation controls the seasonal increase/decrease in satellite observations; the central white area marks the period when ice retreat controls the increase in satellite observations, which comprises the summer period (May-August) during which we assessed DMS emission trends.

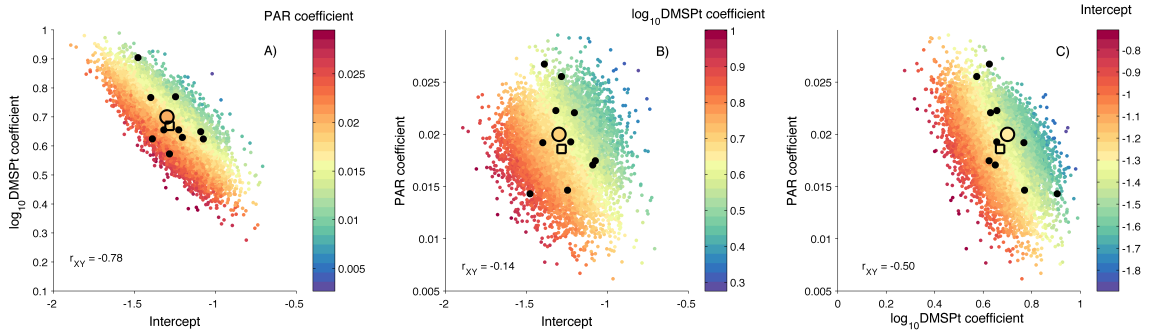

Fig. S2. Bootstrapped eq. 2 coefficients for algorithm tuning and uncertainty assessment. 10^5 sets of bootstrapped regression coefficients were generated for eq. 2 ($\log_{10}DMS = \alpha + \beta \log_{10}DMSPt + \gamma PAR$) for the in situ dataset. Scatterplots display the relationships among the α, β and γ coefficients. In each panel, the square shows the mean coefficient (equivalent to those fitted through regular regression of 5°x5° monthly binned data for latitudes >45°N), the large coloured circle shows the tuned coefficient used for the reference algorithm run (α = –1.3; β = 0.70; γ = 0.020), and the black dots show 10 randomly selected coefficient sets (used to assess the sensitivity of DMS emission to eq. 2 coefficients).

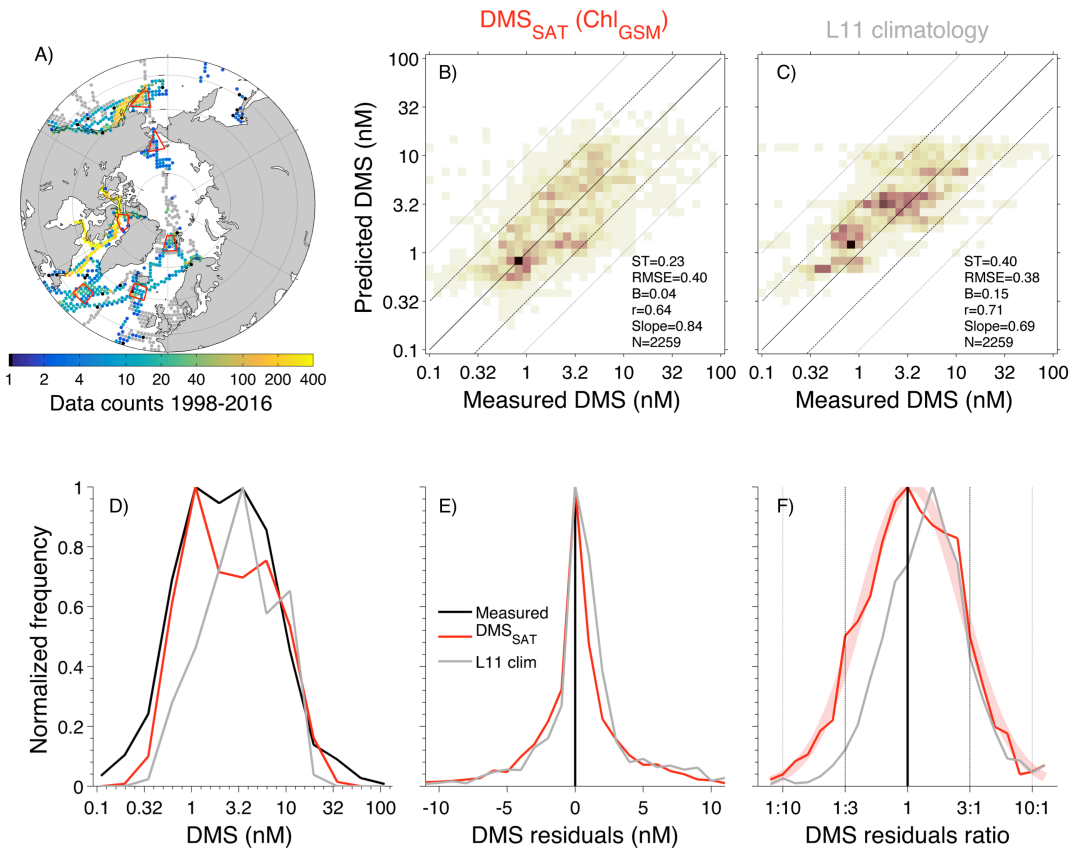

Fig. S3. DMS$_{SAT}$ algorithm validation plots. A) Map of in situ DMS measurements made during the satellite observation period (1998-2016) used to validate our algorithm (data counts calculated within 111 km x 111 km pixels). Gray dots indicate measurements not used for DMS$_{SAT}$ validation (made before 1998). B) Scatterplot of DMS$_{SAT}$ estimates vs. in situ measurements (all binned into 8-day 28 km pixels); darker color indicates higher data density. C) As in (B) but for the L11 DMS climatology. Bottom plots show (D) the probability distribution for the same datasets as above, (E) the linear-space residuals of DMS$_{SAT}$ or L11 vs. in situ data, and (F) the corresponding $\log_{10}$-space residuals, which are equivalent to the estimates/measurements ratio. Residual ratios shown in (F) correspond to the diagonal lines panels (B) and (C).

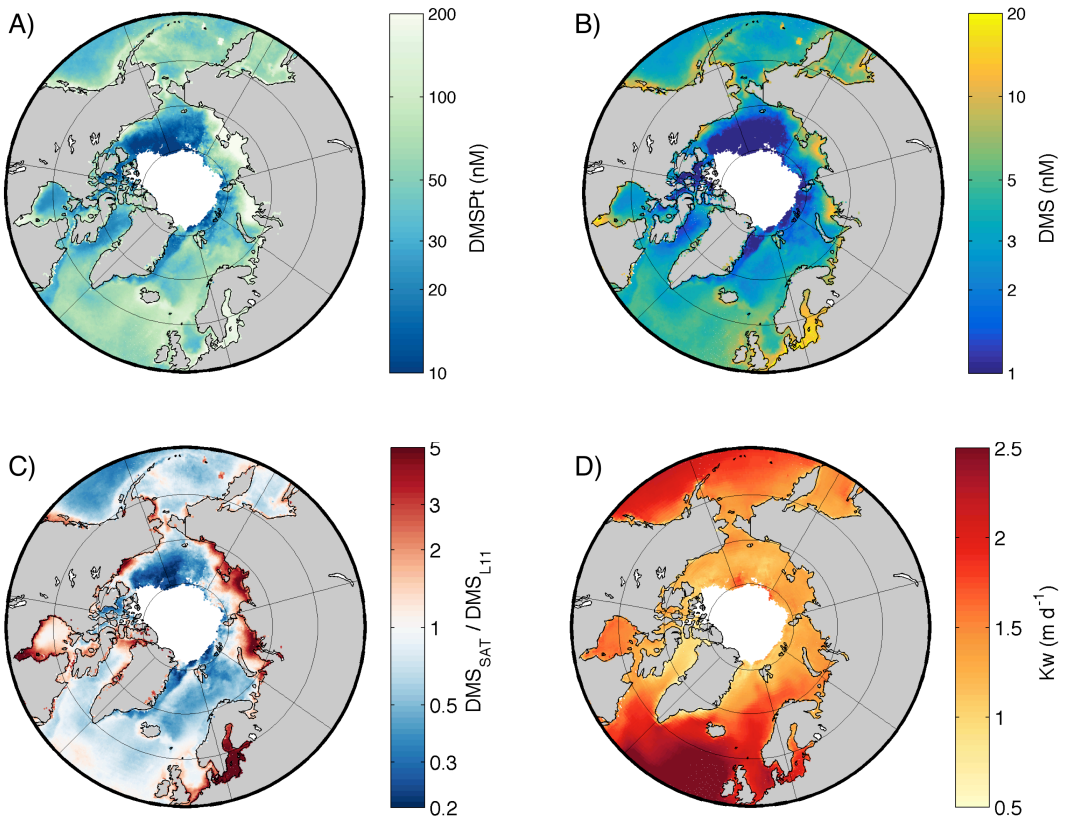

Fig. S4. Mean summertime (May-August) distribution of key variables. Sea surface concentrations, diagnosed with the DMS_{SAT} algorithm, of (A) DMSPt and (B) DMS. C) Ratio between satellite-diagnosed DMS (DMS_{SAT}) and the DMS climatology of Lana et al. 2011 (DMS_{L11}). D) Sea-air gas transfer coefficient (K_w) estimated with the scheme of Woolf 1997 (W97).

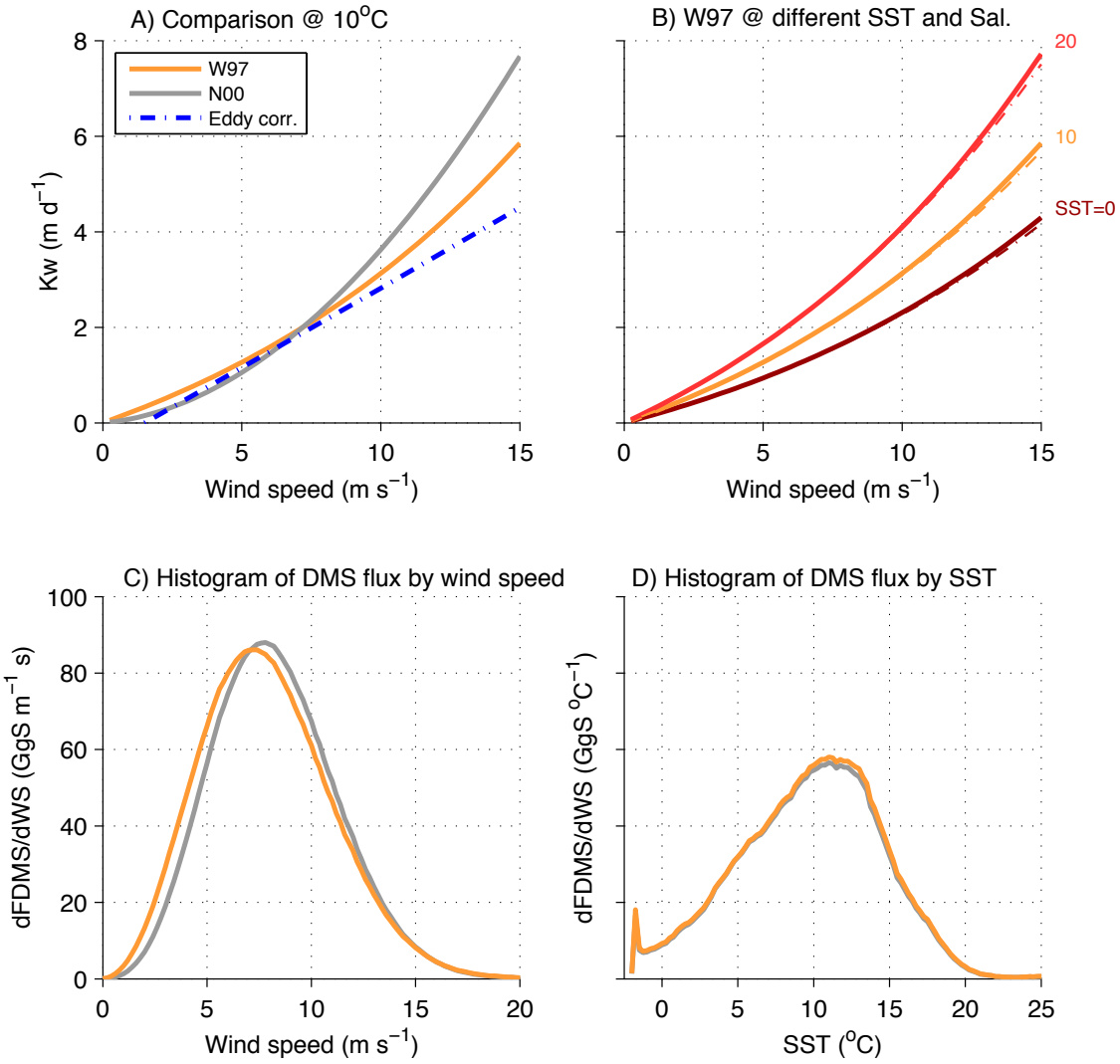

Fig. S5. **Wind-speed and SST-dependence of sea-air DMS transfer coefficients.** A) K_w versus wind speed parameterizations of Woolf 1997 (W97) and Nightingale et al. 2000 (N00); these schemes are compared to a compilation of direct flux measurements made with the eddy correlation technique (31). B) Effect of temperature and salinity on K_w (W97 scheme). Temperatures are indicated on the plot, and salinities are 34 (solid lines) and 20 (dashed lines). C) Frequency distribution of realized DMS emission fluxes at latitudes >45°N (2003-2016, MODIS-Aqua-derived dataset) as a function of wind speed. D) as in (C), but as a function of SST.

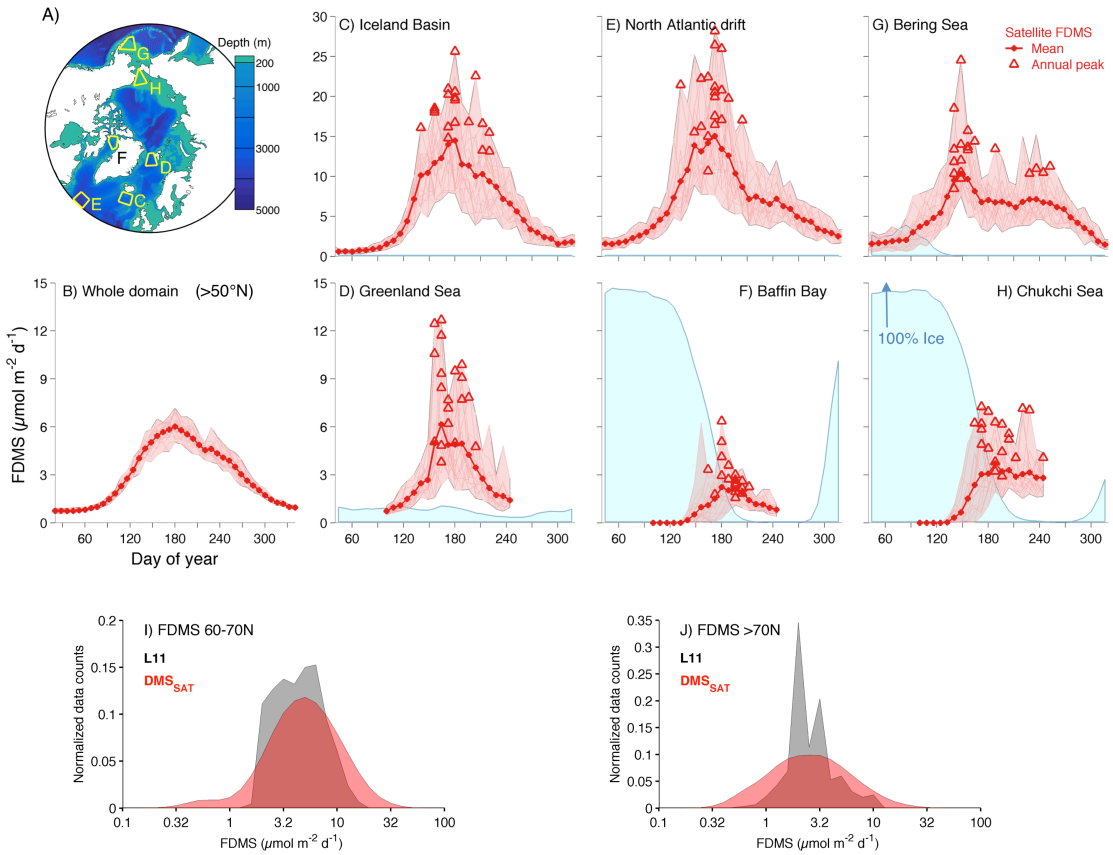

Fig. S6. **DMS flux (FDMS) seasonal cycles and histograms in Subarctic and Arctic seas.** A) Bathymetric map and ecoregions (yellow polygons) used to illustrate DMS dynamics; B-H) mean FDMS seasonal cycle derived from the DMS_{SAT} satellite algorithm for latitudes higher than 50°N (B) and six smaller ecoregions (C-H) shown in panel (A). In (C–H), light red lines mark individual years, light red shadow marks the 19-years envelope, and red triangles mark the annual peak for each year. The light blue shade is the mean fractional ice cover, scaled to the maximum of the y-axis, shown only for regions within the seasonal ice zone. This figure is analogous to Fig. 1 of the main text but, for simplicity, FDMS seasonality estimated using the L11 climatology is not included in (B-H). Bottom panels (I, J) compare histograms of summer FDMS, computed with DMS fields from DMS_{SAT} and L11, and for two latitude bands.

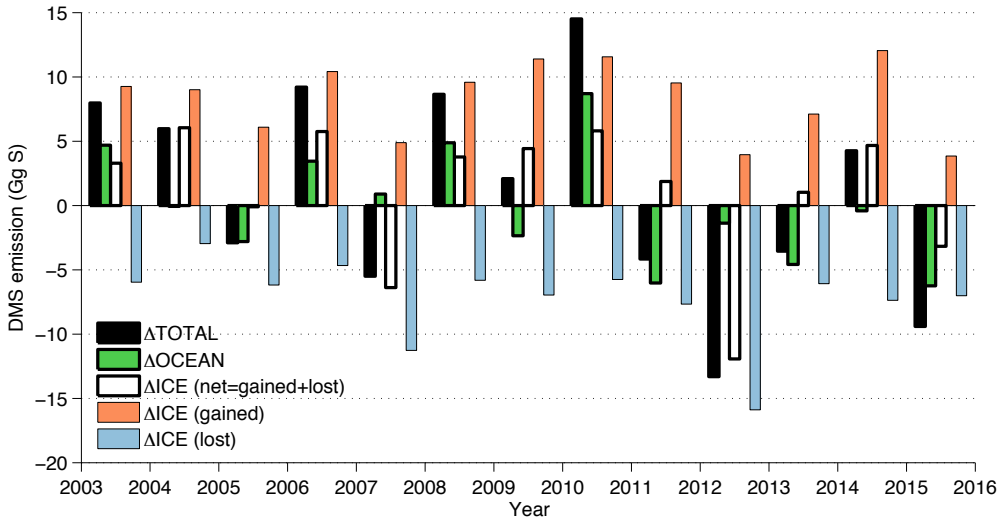

Fig. S7. Decomposition of interannual changes north of 70°N. Interannual changes in DMS emission (EDMS; see Fig. 4), represented by ΔTOTAL, are decomposed into two main components: EDMS change in open-ocean areas (ΔOCEAN, caused by variations in mean FDMS) and EDMS changes caused by shifts in ice patterns (ΔICE, white). The latter results from the net balance between "gained" EDMS (from newly open areas, orange) and "lost" EDMS (newly ice-covered areas, blue) between any two consecutive years.

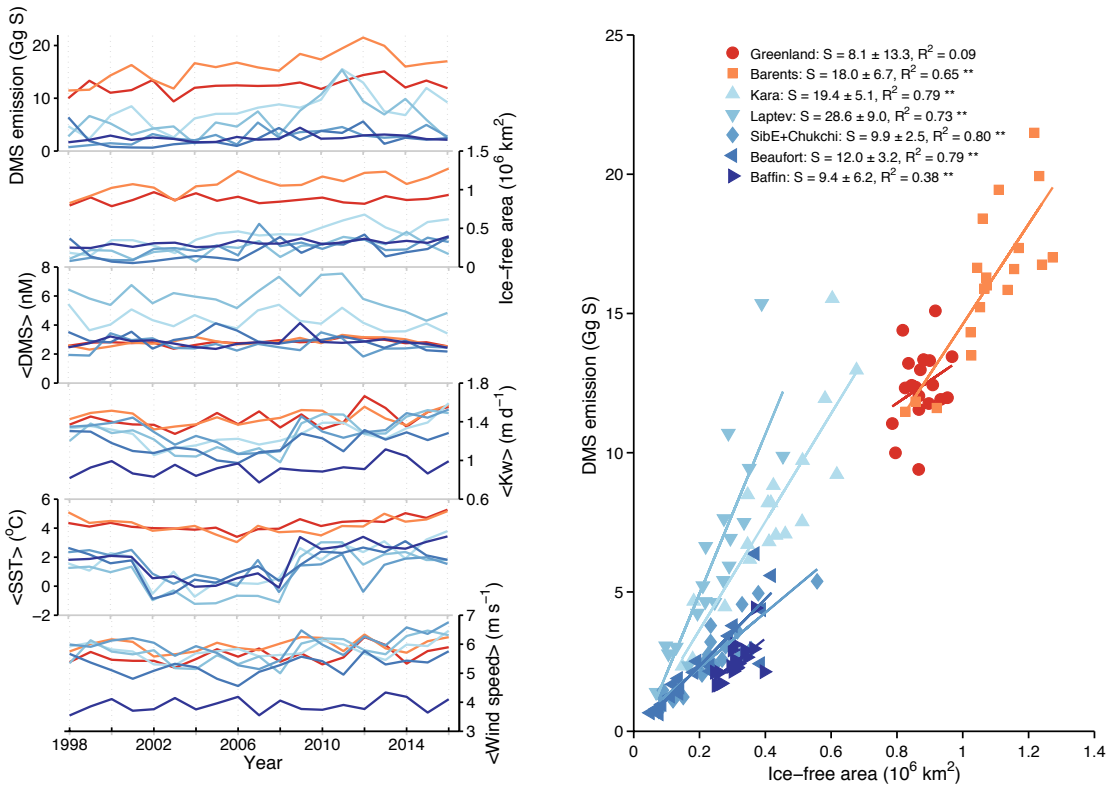

Fig. S8. Regionalized DMS emission (EDMS) and its driving factors north of 70°N (May-August). Data from Fig. 4 of the main paper are here split into 7 sectors. In counterclockwise rotation on a polar projection (Fig. 4 map): Greenland Sea (45°W to 15°E), Barents Sea (15°E to 55°E), Kara Sea (55°E to 105°E), Laptev Sea (105°E to 150°E), East Siberian and Chukchi Seas (150°E to 160°W), Beaufort Sea (160°W to 100°W) and Baffin Bay (100°W to 45°W). The right panel shows regional relationships between summertime EDMS and ice-free area.

Table S1. Summary of recent data sets added to the PMEL database used for algorithm tuning and validation, listed in alphabetical order. Samples deeper than 10 m were excluded.

Reference ***Study area***	**Year (DOY[b])**	**Latitude range**	**Longitude range**	**N**		
				D[a]	**P[a]**	**C[a]**
Galí et al.[c] *Baffin Bay*	2016 (176-192)	68.0–70.5	-64.0– -57.8	47	0	0
Jarnikova et al. (2018), *Canadian Arctic*	2015 (194–230)	51.7–74.8	-105.7– -52.3	32844	294	0
Kameyama et al.[c] *Chukchi Sea*	2015 (249–276)	65.8–74.0	-169.0– -153.6	34	34	24
Kameyama et al.[c] *Chukchi Sea*	2016 (219–232)	65.2–78.5	178.8–180.0	30	30	31
Lizotte et al. 2012 *NW Atlantic*	2003 (115–300)	36.8–59.6	-44.8– -57.7	52	51	48
Lizotte et al.[c] *Baffin Bay and Canadian Arctic*	2014 (198–224)	69.0–81.6	-105.5– -57.9	77	0	0
Lizotte et al.[c] *Baffin Bay and Canadian Arctic*	2016 (205–232)	66.8–80.7	-98.8– -57.1	1022	0	0
Luce et al. 2011 *Canadian Arctic*	2007 and 2008 (280–337)	68.9–76.4	-134.0– -64.5	57	33	19
Matrai et al. 2007 *Barents Sea*	1998, 1999 and 2001 (75–212)	72.5–78.7	31.0–34.4	0	61	32
Merzouk et al. 2006 *NE Pacific*	2002 (191–209)	50.0–51.6	-144.8– -143.0	20	20	0
Royer et al. 2010 *NE Pacific*	2007 (175–195)	48.6–50.0	-145.0– -125.4	11	11	11

[a]D stands for DMS, P for DMSPt, and C for Chl.
[b]day of year (initial–final).
[c]These datasets can be accessed on a public repository (https://doi.org/10.5281/zenodo.3243967).

Table S2. Number of in situ quality-controlled DMS, DMSPt and Chl data (depth < 10 m) at latitudes higher than >45°N. Averaging data into 8-day 28km bins allows for direct comparison against satellite-diagnosed data during the period 1998-2016.

Data source	**Non-binned**						**Binned**		
	1972-2016			**1998-2016**			**1998-2016**		
	D[a]	**P**[a]	**C**[a]	**D**	**P**	**C**	**D**	**P**	**C**
PMEL	15200	1474	1567	11113	469	529	3004	286	421
NEW[b]	34108	398	85	34108	398	85	736	175	48
TOTAL	49308	1872	1652	45221	867	614	3740	461	469

[a]D stands for DMS, P for DMSPt, and C for Chl.

[b]A single high-frequency dataset accounted for over 32000 new measurements prior to binning (Table S1).

Table S3. DMS emission (EDMS) sensitivity tests at latitudes >70°N (MODIS-Aqua sensor only). The reference algorithm (*0. REF*) is compared to alternative algorithm runs where we varied either the DMS sub-algorithm coefficients (eq. 2) (*1. COEFFS*), the Chl product used as input (*2. CHLOC*), or the gas exchange K_w parameterization (*3. KW)*; we also produced alternative emission estimates using climatological DMS fields (*4. REF.CLIM* and *5. L11.CLIM*). Changes with respect to the reference run are shaded in grey. Metrics reported include the mean percentage deviation (MPD) and mean absolute percentage deviation (MAPD) on an annual summer basis, EDMS between 2011 and 2016, and EDMS trends between 2003 and 2016. Asterisks denote significance level: * $\alpha < 0.05$, ** $\alpha < 0.01$.

Algorithm run	**DMS sub-algorithm coeffs.**	**Chl prod.**	**Gas K_w**	**Clim. DMS fields**	**MPD %**	**MAPD %**	**Mean EDMS (2011-2016) Gg S**	**EDMS trend (2003-2016) Gg S decade^{-1}**
0.REF	eq. 2	GSM	W97	NO	0	0	59.7±10.1	13.8±13.0 *
1.COEFFS	bootstrap	GSM	W97	NO	0.1	0.8	59.6±10.4	13.4±4.1 *
2.CHLOC	eq. 2	OC3M	W97	NO	-2.5	7.9	58.5±5.5	16.9±6.9 **
3.KW	eq. 2	GSM	N00	NO	-1.7	1.7	59.3±10.3	14.9±13.4 *
4.REF.CLIM	eq. 2	GSM	W97	YES	3.3	8.0	62.4±5.6	19.2±7.6 **
5.L11.CLIM	na	na	W97	YES	37.0	37.0	77.6±6.7	16.3±7.7 **

na: not applicable.

References

1. Galí M, Devred E, Levasseur M, Royer S-J, Babin M (2015) A remote sensing algorithm for planktonic dimethylsulfoniopropionate (DMSP) and an analysis of global patterns. *Remote Sens Environ* 171:171–184.
2. NASA Goddard Space Flight Center, Ocean Ecology Laboratory, Ocean Biology Processing Group. Moderate-resolution Imaging Spectroradiometer (MODIS) Aqua Ocean Color Data; 2014 Reprocessing (accessed on December 5, 2016) (2014).
3. Schmidtko S, Johnson GC, Lyman JM (2013) MIMOC: A global monthly isopycnal upper-ocean climatology with mixed layers. *J Geophys Res Ocean* 118(4):1658–1672.
4. Cavalieri DJ, Parkinson CL, Gloersen P, Zwally HJ (1996) *Sea Ice Concentrations from Nimbus-7 SMMR and DMSP SSM/I-SSMIS Passive Microwave Data, Version 1. Subset used: 1998 to 2015.* (Boulder, Colorado USA.).
5. Maslanik J, Stroeve J (1999) *Near-Real-Time DMSP SSMIS Daily Polar Gridded Sea Ice Concentrations, Version 1. Subset used: 2016.* (Boulder, Colorado USA.).
6. Dee DP, et al. (2011) The ERA-Interim reanalysis: Configuration and performance of the data assimilation system. *Q J R Meteorol Soc* 137(656):553–597.
7. Maritorena S, Siegel DA, Peterson AR (2002) Optimization of a semianalytical ocean color model for global-scale applications. *Appl Opt* 41(15):2705–2714.
8. O'Reilly JE, et al. (1998) Ocean color chlorophyll algorithms for SeaWiFS. *J Geophys Res* 103(C11):24937–24953.
9. Ben Mustapha S, Bélanger S, Larouche P (2012) Evaluation of ocean color algorithms in the southeastern Beaufort Sea, Canadian Arctic: New parameterization using SeaWiFS, MODIS, and MERIS spectral bands. *Can J Remote Sens* 38(5):535–556.
10. Lee ZP, Du KP, Arnone R (2005) A model for the diffuse attenuation coefficient of downwelling irradiance. *J Geophys Res C Ocean* 110(2):1–10.
11. Broerse ATC, et al. (2003) The cause of bright waters in the Bering Sea in winter. *Cont Shelf Res* 23(16):1579–1596.
12. Cota GF, Wang J, Comiso JC (2004) Transformation of global satellite chlorophyll retrievals with a regionally tuned algorithm. *Remote Sens Environ* 90:373–377.
13. Jolliff JK, et al. (2009) Summary diagrams for coupled hydrodynamic-ecosystem model skill assessment. *J Mar Syst* 76(1–2):64–82.
14. Lee YJ, et al. (2015) An assessment of phytoplankton primary productivity in the Arctic Ocean fromsatellite ocean color/in situ chlorophyll-a basedmodels. *J Geophys Res Ocean* 120.
15. Land PE, Shutler JD, Bell TG, Yang M (2014) Exploiting satellite earth observation to quantify current global oceanic DMS flux and its future climate sensitivity. *J Geophys Res Ocean* 119(11):7725–7740.
16. Johnson MT (2010) A numerical scheme to calculate temperature and salinity dependent air-water transfer velocities for any gas. *Ocean Sci* 6(4):913–932.
17. Liss PS, Slater PG (1974) Flux of Gases across the Air-Sea Interface. *Nature* 247:181–184.
18. Goddijn-Murphy L, Woolf DK, Marandino C (2012) Space-based retrievals of air-sea gas transfer velocities using altimeters: Calibration for dimethyl sulfide. *J Geophys Res* 117(C8):C08028.
19. Wanninkhof R, Asher WE, Ho DT, Sweeney C, McGillis WR (2009) Advances in Quantifying Air-Sea Gas Exchange and Environmental Forcing. *Ann Rev Mar Sci* 1(1):213–244.
20. Saltzman ES, King DB, Holmen K, Leck C (1993) Experimental Determination of the Diffusion Coefficient of Dimethylsulfide in Water. *J Geophys Res* 98(C9):16481–16486.
21. Nightingale PD, et al. (2000) In situ evaluation of air-sea gas exchange parameterizations

using novel conservative and volatile tracers. *Global Biogeochem Cycles* 14(1):373–387.
22. Woolf DK (1997) *Bubbles and their role in gas exchange*.
23. Tesdal J-E, Christian JR, Monahan AH, von Salzen K (2016) Evaluation of diverse approaches for estimating sea-surface DMS concentration and air-sea exchange at global scale. *Environ Chem* 13:390–412.
24. Kettle AJ, et al. (1999) A global data base of sea surface dimethylsulfide (DMS) measurements and a simple model to predict sea surface DMS as a function of latitude, longitude, and month. *Glob Biogeochem Cycles* 13(2):399–444.
25. Simó R, Dachs J (2002) Global ocean emission of dimethylsulfide predicted from biogeophysical data. *Global Biogeochem Cycles* 16(4):1078.
26. Schwinger J, et al. (2017) Amplification of global warming through pH-dependence of DMS-production simulated with a fully coupled Earth system model. *Biogeosciences* 14:3633–3648.
27. Wang S, Maltrud M, Burrows S, Elliott S, Smith PC (2018) Impacts of shifts in phytoplankton community on clouds and climate via the sulfur cycle. *Global Biogeochem Cycles* 32:1005–1026.
28. Wang S, Maltrud M, Elliott S, Cameron-Smith P, Jonko A (2018) Influence of dimethyl sulfide on the carbon cycle and biological production. *Biogeochemistry* 138(1):49–68.
29. Fiddes SL, Woodhouse MT, Nicholls Z, Lane TP, Schofield R (2018) Cloud, precipitation and radiation responses to large perturbations in global dimethyl sulfide. *Atmos Chem Phys* 18:10177–10198.
30. Tesdal JE, Christian JR, Monahan AH, Von Salzen K (2016) Sensitivity of modelled sulfate aerosol and its radiative effect on climate to ocean DMS concentration and air-sea flux. *Atmos Chem Phys* 16(17):10847–10864.
31. Bell TG, et al. (2015) Dimethylsulfide gas transfer coefficients from algal blooms in the Southern Ocean. *Atmos Chem Phys* 15(4):1783–1794.